Investigation of the high-frequency attenuation parameter, κ (kappa), from aftershocks of the 2010 M_w 8.8 Maule, Chile earthquake

C. Neighbors,[1] E. J. Liao,[1] E. S. Cochran,[2] G. J. Funning,[1] A. I. Chung,[3]
J. F. Lawrence,[3] C. Christensen,[3] M. Miller,[4] A. Belmonte[4] and H. H. Andrés Sepulveda[4]

[1]*Department of Earth Sciences, University of California, Riverside, CA 92521, USA. E-mail: corrie.neighbors@email.ucr.edu*
[2]*Earthquake Science Center, US Geological Survey, Pasadena, CA 91106, USA*
[3]*School of Earth Sciences, Stanford University, Stanford, CA 94305, USA*
[4]*Departamento de Geofísica, Universidad de Concepción, Concepción, Chile*

SUMMARY

The Bío Bío region of Chile experienced a vigorous aftershock sequence following the 2010 February 27 M_w 8.8 Maule earthquake. The immediate aftershock sequence was captured by two temporary seismic deployments: the Quake Catcher Network Rapid Aftershock Mobilization Program (QCN RAMP) and the Incorporated Research Institutions for Seismology CHile Aftershock Mobilization Program (IRIS CHAMP). Here, we use moderate to large aftershocks ($M_\mathrm{L} \geq 4.0$) occurring between 2010 March 1 and June 30 recorded by QCN RAMP and IRIS CHAMP stations to determine the spectral decay parameter, kappa (κ). First, we compare waveforms and κ estimates from the lower-resolution QCN stations to the IRIS CHAMP stations to ensure the QCN data are of sufficient quality. We find that QCN stations provide reasonable estimates of κ in comparison to traditional seismic sensors and provide valuable additional observations of local ground motion variation. Using data from both deployments, we investigate the variation in κ for the region to determine if κ is influenced primarily by local geological structure, path attenuation, or source properties (e.g. magnitude, mechanism and depth). Estimates of κ for the Bío Bío region range from 0.0022 to 0.0704 s with a mean of 0.0295 s and are in good agreement with κ values previously reported for similar tectonic environments. κ correlates with epicentral distance and, to a lesser degree, with source magnitude. We find little to no correlation between the site kappa, κ_0, and mapped geology, although we were only able to compare the data to a low-resolution map of surficial geology. These results support an increasing number of studies that suggest κ observations can be attributed to a combination of source, path and site properties; additionally, measured κ are often highly scattered making it difficult to separate the contribution from each of these factors. Thus, our results suggest that contributions from the site, path and source should be carefully considered when interpreting κ values.

Key words: Earthquake ground motions; Body waves; Seismic attenuation.

1 INTRODUCTION

The Peru-Chile subduction zone is one of the most seismically hazardous regions in the world and is characterized by the young oceanic Nazca Plate subducting beneath the continental South American Plate. Convergence of the two plates occurs at an estimated rate of 6–9 cm yr^{-1} in the N78°E direction resulting in earthquakes along the interface of the plate boundary as well as within the downgoing subducting slab (e.g. DeMets *et al.* 1990; Arango *et al.* 2011). Historically, events in the Peru-Chile subduction zone have been large and relatively frequent, with 17 events of

magnitude greater than 7.5 observed in the last 50 yr (e.g. Arango *et al.* 2011).

Here, we investigate attenuation and site response in the Bío Bío region, an administrative division (i.e. state) of Chile, located in the central portion of the country. The coastal Bío Bío area is a region of high seismic hazard due to the proximity of the active offshore Peru-Chile subduction zone, as described above. The 2010 M_w 8.8 Maule, Chile earthquake caused extensive damage in Bío Bío, particularly to the region's capital city of Concepción. Spatial variations in subsurface geological material can result in spatially variable ground motion, and also damage, during an earthquake. These so-called

'site effects' are a local response of seismic waves to subsurface structure and geological material. Site effects represent the mean response of a site to many moderate to large earthquake events; thus variability due to seismic ray incidence angles, azimuthal directions and seismic waves types are averaged (e.g. Boore 2004). It has been proposed that by incorporating high frequency attenuation information into regional attenuation functions and ground motion prediction equations (GMPEs), it may be possible to better predict ground motions from earthquakes at a location (e.g. Cotton *et al.* 2006; Akkar *et al.* 2012; Laurendeau *et al.* 2013).

Kappa, κ, is defined as the fall-off of the high frequency (typically >1 Hz) Fourier amplitude spectrum (e.g. Anderson & Hough 1984; Anderson 1986; Castro *et al.* 1990; Douglas *et al.* 2010). This exponential decay in high-frequency energy is proposed to primarily reflect source-station attenuation and local site response (e.g. Anderson & Hough 1984; Ktenidou *et al.* 2013). The shape of the Fourier acceleration spectrum at high frequencies of seismograms can be described by

$$a(f) = A_0 \exp(-\pi \kappa f) \quad \text{for} \quad f > f_E, \tag{1}$$

where f_E is a frequency just above the corner frequency, f_c, above which the decay is approximately linear in $(f, \log[a(f)])$ space and A_0 is a source- and path-dependent amplitude. The above eq. (1) assumes a frequency-independent Q, where Q is a dimensionless parameter that describes the energy loss per cycle of oscillation (e.g. Knopoff 1964; Lay & Wallace 1995; Campbell 2009).

An investigation of κ values is important in regions such as Chile, where the seismic monitoring network is sparse and the seismic hazard associated with future earthquakes has large uncertainties due limited knowledge of expected ground motion. Observational studies have shown that there is significant variability in ground motion for a single earthquake recorded at multiple sites as well as for records of many earthquakes recorded at a single site. While κ describes the attenuation of the amplitude spectrum at a site, there is continuing debate over the predominant mechanism that controls this fall off of high frequencies (e.g. Hanks 1982; Anderson & Hough 1984; Tsai & Chen 2000; Purvance & Anderson 2003). Initial studies (e.g. Anderson & Hough 1984; Anderson 1991) found that the estimation of the κ value is correlated to the geological material at a site, identified as site kappa κ_0, such that high κ_0 values indicate high attenuation and therefore lower shear wave velocities, V_s, typical of subsurface sedimentary or alluvial material. Conversely, low κ_0 values at a station location may indicate less attenuation and more competent rock. However, this relationship has not been consistent across the regions and seismic events studied. A number of studies propose that κ is primarily due to site effects (e.g. Hanks 1982; Anderson & Hough 1984; Rovelli *et al.* 1988; Anderson 1991). Researchers have also proposed there are relationships between κ and source–receiver distance (e.g. Anderson & Hough 1984; Castro *et al.* 2000; Douglas *et al.* 2010), size, mechanism and/or depth of the source (e.g. Papageorgiou & Aki 1983; Purvance & Anderson 2003; Parolai & Bindi 2004) and some combination of the above (e.g. Tsai & Chen 2000; Kilb *et al.* 2012).

While κ studies generally report a positive relationship between κ and distance, these studies also show considerable scatter in κ values. Variation in site kappa values with source-to-station azimuths has also been documented with greater than 5 per cent differences between the average κ estimated in two azimuthal bins (Gentili & Franceschina 2011). And, while most researchers have found a correlation between κ and site geology, the results are not always robust. Discrepancies between site kappa values, κ_0, and near-surface geology have been attributed to possible topographic effects, the

non-linear behaviour of geological material, varying depth and thickness of sediment and bedrock columns and variations in Q structure (e.g. Castro *et al.* 2000; Parolai & Bindi 2004; Campbell 2009; Edwards *et al.* 2011). As mentioned, some studies have found a relationship between κ values and the source (e.g. Castro *et al.* 2000; Purvance & Anderson 2003). Specifically, Kilb *et al.* (2012) suggest κ values are influenced by source or near-source properties and Purvance & Anderson (2003) found that κ estimates increase with magnitude. Also, Purvance & Anderson (2003) report a relationship between κ and source mechanism, such that normal faulting events have lower κ values than thrust events. Thus, while there is some agreement amongst studies in characterizing the behaviour of high-frequency attenuation, it has not been wholly conclusive.

Here, we measure κ for waveforms recorded by the QCN and IRIS CHAMP stations deployed following the M_w 8.8 Maule, Chile earthquake. We then determine the influence of distance, magnitude, depth and surficial geology on the high frequency response, κ.

2 DATA

The majority of aftershocks used in this study occurred offshore within the zone of coseismic slip parallel to the trench with predominant shallow thrust mechanisms (e.g. Lange *et al.* 2012). The sequence was captured by two temporary seismic deployments: the Quake Catcher Network Rapid Aftershock Mobilization Program (QCN RAMP) and the Incorporated Research Institutions for Seismology CHile Aftershock Mobilization Program (IRIS CHAMP). The Quake Catcher Network (QCN) uses low-cost (<\$150) Micro-Electro-Mechanical System (MEMS) accelerometers that are connected to a computer via Universal Serial Bus (USB). Sensors are attached to the floor, oriented with one horizontal component aligned with North. The sensors are monitored using the distributed computing software, BOINC (Berkeley Open Infrastructure for Network Computing; Anderson 2004), which uses a participant's unused central processing units (CPUs) to detect local strong ground motion (for more information on QCN sensors and network design, see Cochran *et al.* 2009a,b and Evans *et al.* 2014). By utilizing the idle time of a growing number of computers, QCN has effectively created a dense network of (low-resolution) seismic monitoring stations at 1 per cent of the cost of a traditional array. In this study we deployed several models of triaxial MEMS sensors (10-, 12-, 14-bit and prototype 16-bit) with a dynamic range of $\pm 2\,g$ (where g is Earth's gravity, 9.81 m s^{-2}; thus 2 g is 19.62 m s^{-2}) and have resolutions, depending on sensor type, of 0.06–4 mg (5.89×10^{-4} to 3.92×10^{-2} m s^{-2}). Laboratory experiments of standard linear shake table tests show that QCN sensors provide reliable amplitude and frequency measurements where the instrument response of the sensors is essentially flat from 0 Hz to the Nyquist frequency (25 Hz; Evans *et al.* 2014). In addition, Cochran *et al.* (2011) find that QCN sensors yield similar ground motion records to traditional strong motion stations for analogous deployment conditions. Waveforms are recorded at 50 samples per second (sps).

Following the 2010 February 27 M_w 8.8 Maule, Chile earthquake, colleagues from QCN and the University of Concepción deployed roughly 100 USB sensors in the city of Concepción, the urban centre closest to the epicentre, and the surrounding Bío Bío region. This location was chosen due to its proximity to the epicentre and expected aftershocks as well as its concentration of infrastructure to ensure enough volunteers would be available to host sensors. Due to computer processing and internet connectivity requirements, individual sensor locations were largely based on availability of volunteer com-
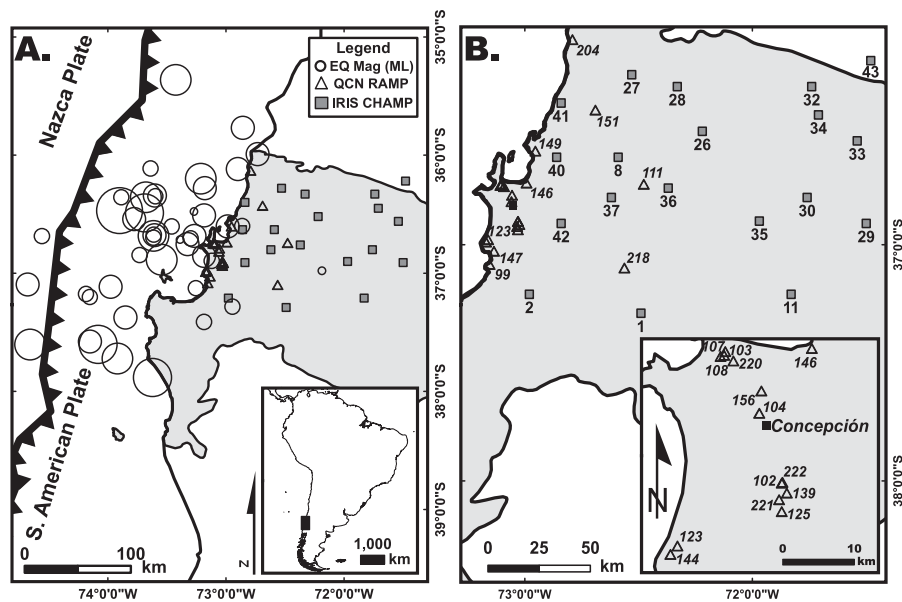
Figure 1. (a) Tectonic setting of study area overlaid with aftershocks (circles, scaled by magnitude) and seismic stations (squares, triangles) used in analysis. Bío Bío region within Chile is shaded grey. Inset shows study area (black rectangle) on the western coast of South America. (b) Seismic network map of QCN RAMP stations (triangles) and IRIS CHAMP stations (grey squares). Location of regional capital, Concepción, plotted as a black square. Inset map shows enlargement of the greater Concepción area where many QCN stations are located.
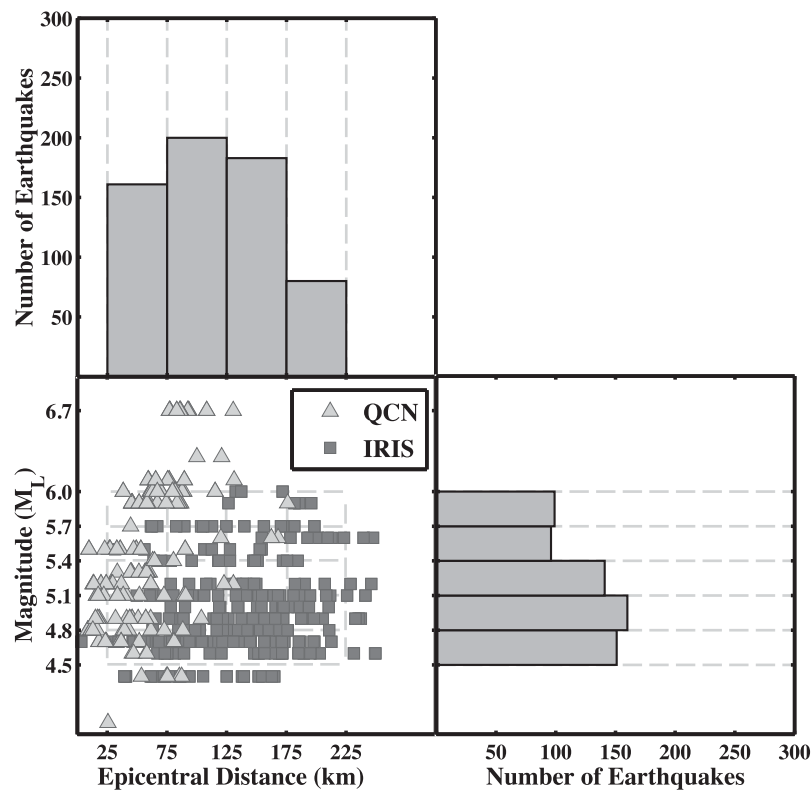
Figure 2. Magnitude and epicentral distance distribution of earthquakes used in this analysis. Dashed lines represent grid intervals used in the distance, magnitude inversion.

puters (further details of the QCN RAMP Chile deployment can be found in Chung *et al.* 2011). During the deployment period, the QCN network captured over 229 earthquakes ($4.0 \leq M_L \leq 6.7$) from 2010 March 1 to June 30 at epicentral distances ranging from 9 to 176 km (Figs 1 and 2; Table 1). Earthquake location, local

magnitude and depth were obtained from the Centro Sismológico Nacional at the Universidad de Chile (http://www.sismologia.cl/).

In addition to data collected by QCN, we also use data recorded by the IRIS CHAMP seismic network (Meltzer *et al.* 2010). IRIS collaborators from the United States worked with research scientists at

Table 1. List of temporary seismic stations and characteristics of the earthquake-station data. QCN RAMP stations marked by asterisks (*). Earthquake size and epicentral distance ranges recorded by each station are given. The average kappa κ_{ave} observed at the station, distance-dependence $\kappa_0^r(z)$ values, and site geology class are noted. The uncertainty in $\kappa_0^{r,M}(z)$ is determined by a bootstrap random resampling with replacement procedure. The average κ_0^r is 0.0223 ± 0.00686 s, where Hard Rock has an average of 0.0223 ± 0.00797 s, Soft Rock 0.0235 ± 0.00463 s, and Sediment has an average of 0.0217 ± 0.00690 s. The average $\kappa_0^{r,M}$ is 0.0209 ± 0.00711 s, where Hard Rock has an average of 0.0219 ± 0.00833 s, Soft Rock 0.0208 ± 0.00526 s, and Sediment has an average of 0.0200 ± 0.00685 s. Note that there is no $\kappa_0^{r,M}$ estimate is available for QCN station 151 as data points lay outside of the magnitude-distance grid.

| Station	Latitude	Longitude	Recorded earthquakes	EQ M_L range	Epicentral distance range (km)	κ_{ave} (s)	κ_0^r (s)	$\kappa_0^{r,M}$ (s)	Geology group
99*	−37.08	−73.15	3	5.3–6.3	60.2–100.1	0.0273 ± 0.0025	0.0226 ± 0.0005	0.0233 ± 0.0034	Soft Rock
102*	−36.90	−73.03	4	5.3–5.9	33.5–120.2	0.0220 ± 0.0029	0.0179 ± 0.0029	0.0159 ± 0.0021	Hard Rock
103*	−36.75	−73.10	5	4.8–6.7	16.5–77.5	0.0250 ± 0.0084	0.0216 ± 0.0047	0.0163 ± 0.0039	Soft Rock
104*	−36.82	−73.06	3	5.5–6.0	35.9–75.3	0.0253 ± 0.0056	0.0216 ± 0.0066	0.0193 ± 0.0023	Sediment
107*	−36.74	−73.10	16	4.0–6.0	16.1–85.5	0.0242 ± 0.0077	0.0215 ± 0.0038	0.0213 ± 0.0026	Soft Rock
108*	−36.75	−73.11	7	5.3–6.7	27.3–77.2	0.0330 ± 0.0047	0.0295 ± 0.0049	0.0254 ± 0.0029	Soft Rock
111*	−36.74	−72.48	3	4.8–6.7	72.8–130.6	0.0224 ± 0.0070	0.0161 ± 0.0062	0.0152 ± 0.0039	Sediment
123*	−36.98	−73.16	7	4.8–6.0	9.9–86.6	0.0188 ± 0.0055	0.0158 ± 0.0029	0.0131 ± 0.0020	Sediment
125*	−36.94	−73.03	9	4.8–6.7	9.1–93.3	0.0234 ± 0.0061	0.0193 ± 0.0030	0.0178 ± 0.0025	Hard Rock
139*	−36.91	−73.02	15	4.4–6.7	8.8–176.1	0.0228 ± 0.0088	0.0181 ± 0.0043	0.0174 ± 0.0031	Hard Rock
144*	−36.99	−73.17	8	4.4–6.0	11.3–87.7	0.0163 ± 0.0087	0.0131 ± 0.0051	0.0120 ± 0.0024	Sediment
146*	−36.74	−72.99	4	5.2–6.7	29.6–86.3	0.0379 ± 0.0043	0.0335 ± 0.0072	0.0305 ± 0.0034	Hard Rock
147*	−37.03	−73.14	3	4.6–4.9	15.1–57.6	0.0173 ± 0.0148	0.0151 ± 0.0182	0.0126 ± 0.0018	Soft Rock
149*	−36.60	−72.95	4	5.1–6.7	22.9–85.8	0.0269 ± 0.0122	0.0234 ± 0.0103	0.0178 ± 0.0009	Soft Rock
151*	−36.43	−72.69	3	4.7–6.7	24.5–108.3	0.0379 ± 0.0142	0.0325 ± 0.0070	– ± –	Sediment
156*	−36.79	−73.06	15	4.7–6.7	13.0–168.2	0.0288 ± 0.0111	0.0251 ± 0.0041	0.0204 ± 0.0025	Soft Rock
204*	−36.13	−72.79	3	5.1–6.0	9.7–38.5	0.0312 ± 0.0072	0.0295 ± 0.0078	0.0279 ± 0.0052	Sediment
218*	−37.10	−72.56	4	4.8–6.0	39.5–115.4	0.0108 ± 0.0046	0.0059 ± 0.0051	0.0075 ± 0.0020	Hard Rock
220*	−36.75	−73.09	7	4.6–5.4	13.7–90.7	0.0317 ± 0.0087	0.0292 ± 0.0052	0.0292 ± 0.0035	Soft Rock
221*	−36.92	−73.03	11	4.4–6.0	33.5–162.5	0.0327 ± 0.0055	0.0276 ± 0.0034	0.0282 ± 0.0036	Hard Rock
222*	−36.90	−73.03	4	4.4–6.0	32.0–80.5	0.0227 ± 0.0034	0.0182 ± 0.0068	0.0197 ± 0.0029	Hard Rock
01	−37.29	−72.49	17	4.7–5.7	63.0–194.9	0.0220 ± 0.0057	0.0135 ± 0.0032	0.0134 ± 0.0022	Hard Rock
02	−37.21	−72.98	11	4.4–5.7	61.6–154.5	0.0374 ± 0.0095	0.0310 ± 0.0057	0.0321 ± 0.0025	Hard Rock
08	−36.63	−72.59	12	4.4–5.7	60.7–213.0	0.0335 ± 0.0132	0.0272 ± 0.0069	0.0278 ± 0.0024	Hard Rock
11	−37.21	−71.83	17	4.4–5.7	40.8–249.3	0.0294 ± 0.0102	0.0195 ± 0.0068	0.0186 ± 0.0031	Sediment
26	−36.52	−72.22	9	4.4–5.7	58.0–247.6	0.0343 ± 0.0107	0.0262 ± 0.0071	0.0282 ± 0.0025	Hard Rock
27	−36.28	−72.53	7	4.7–5.7	46.4–239.7	0.0299 ± 0.0104	0.0217 ± 0.0062	0.0214 ± 0.0022	Hard Rock
28	−36.33	−72.33	19	4.4–5.7	56.1–225.9	0.0233 ± 0.0099	0.0155 ± 0.0050	0.0156 ± 0.0025	Sediment
29	−36.91	−71.50	20	4.4–6.0	61.5–246.2	0.0219 ± 0.0102	0.0109 ± 0.0067	0.0058 ± 0.0029	Hard Rock
30	−36.80	−71.76	11	4.4–5.4	100.7–249.6	0.0383 ± 0.0084	0.0280 ± 0.0069	0.0305 ± 0.0025	Sediment
32	−36.33	−71.74	20	4.4–6.0	82.4–235.7	0.0420 ± 0.0132	0.0321 ± 0.0084	0.0315 ± 0.0028	Sediment
33	−36.56	−71.54	8	4.4–5.4	118.1–210.9	0.0396 ± 0.0099	0.0289 ± 0.0142	0.0261 ± 0.0025	Sediment
34	−36.45	−71.71	19	4.4–6.0	72.6–232.8	0.0292 ± 0.0094	0.0194 ± 0.0061	0.0192 ± 0.0027	Sediment
35	−36.90	−71.97	14	4.4–5.7	86.1–241.4	0.0342 ± 0.0093	0.0244 ± 0.0054	0.0236 ± 0.0029	Sediment
36	−36.76	−72.37	18	4.4–5.9	47.3–223.4	0.0255 ± 0.0070	0.0168 ± 0.0030	0.0165 ± 0.0030	Sediment
37	−36.80	−72.62	6	4.6–5.6	30.9–201.4	0.0356 ± 0.0141	0.0280 ± 0.0057	0.0280 ± 0.0022	Hard Rock
40	−36.63	−72.86	12	4.4–5.7	3.2–192.7	0.0319 ± 0.0081	0.0260 ± 0.0032	0.0259 ± 0.0028	Hard Rock
41	−36.40	−72.84	18	4.4–5.9	31.8–209.7	0.0290 ± 0.0104	0.0224 ± 0.0042	0.0224 ± 0.0022	Sediment
42	−36.91	−72.84	6	4.6–5.7	34.4–178.4	0.0386 ± 0.0067	0.0322 ± 0.0035	0.0308 ± 0.0032	Hard Rock
43	−36.22	−71.48	12	4.4–5.7	105.4–212.8	0.0222 ± 0.0098	0.0109 ± 0.0134	0.0087 ± 0.0021	Sediment

the University of Chile, Santiago to deploy 60 PASSCAL (Program for Array Seismic Studies of the Continental Lithosphere) stations from mid-March to mid-September (http://www.iris.edu/hq/chile/). The PASSCAL instruments were installed throughout central Chile, with roughly 20 stations in the Bío Bío region. These broadband Güralp CMG-3T instruments can produce higher resolution records than the QCN stations, but are also more costly in terms of time and money to ship and deploy. The PASSCAL instruments were transported to Chile by the U.S. military's Southern Command (SouthCom) and arrived roughly two weeks after the main shock. In contrast, within three days of the M_w 8.8 earthquake 100 QCN sensors were transported by plane in two pieces of checked luggage. The ability to rapidly deploy sensors resulted in QCN RAMP recording at least 22 additional aftershocks, most notably the large M_L 6.7 aftershock, local to the Bío Bío region during the early aftershock period. The IRIS network captured over 35 earthquakes ($4.4 \leq M_L \leq 6.0$) from 2010 March 21 to June 30 at epicentral distances ranging from 3 to 250 km (Figs 1 and 2; Table 1). IRIS CHAMP stations were set to record continuously at 100 sps. Some QCN and IRIS stations in Concepción and Bío Bío experienced power issues and data gaps during the duration of our study and were excluded. As the QCN stations are lower resolution [i.e. fewer bit count poorly resolves small signals and results in lower signal-to-noise ratios (SNR)], the IRIS CHAMP data are needed to first verify if the low-cost QCN accelerometers can be reliably used to estimate κ and then, using both networks, we explore κ estimates for the region.

3 METHODS

Following the method and terminology outlined in Douglas *et al.* (2010) (adapted from Anderson & Hough 1984), we use seismograms of earthquakes of magnitude 4.0 or greater recorded on horizontal components of the QCN and IRIS CHAMP sensors during the period of 2010 March 1 to June 30. For each record, the mean is removed and then the time-series is visually inspected for clarity of *P*- and *S*-wave arrivals; noisy or other poor quality records are discarded from further analysis. The *P*-wave and *S*-wave arrivals are manually picked and 5 s time windows of direct *S*-wave and pre-event noise (30 s prior to *S*-wave arrival) are cut from the length of the record and tapered using a 5 per cent Hanning taper (Fig. 3a). For κ analysis, the window length used should have little effect as long as the energetic parts of the *S* waves are captured (Tsai & Chen 2000; Douglas *et al.* 2010). We do not rotate the seismograms to radial and transverse components as we assume that the spectra represent the average response of the site. It has been shown at high frequencies, such as those considered here, scattering averages out the radiation pattern; thus the two horizontals may be averaged and are interchangeable for our purpose (Castro *et al.* 1990). We investigate this assumption by comparing κ estimates for source–receiver pairs and find that the percent difference is on average 22.5 per cent with a median of 14.4 per cent for the two horizontal components. This is less than the average percentage difference for κ estimates at each station, thus we feel this assumption is acceptable for our analysis.

The Fourier spectra of the pre-event and *S*-wave time windows are computed and plotted on a semilog plot (Figs 3b and c). A line is fit to the slope by the relationship

$$\kappa = -\frac{\lambda}{\pi}, \tag{2}$$
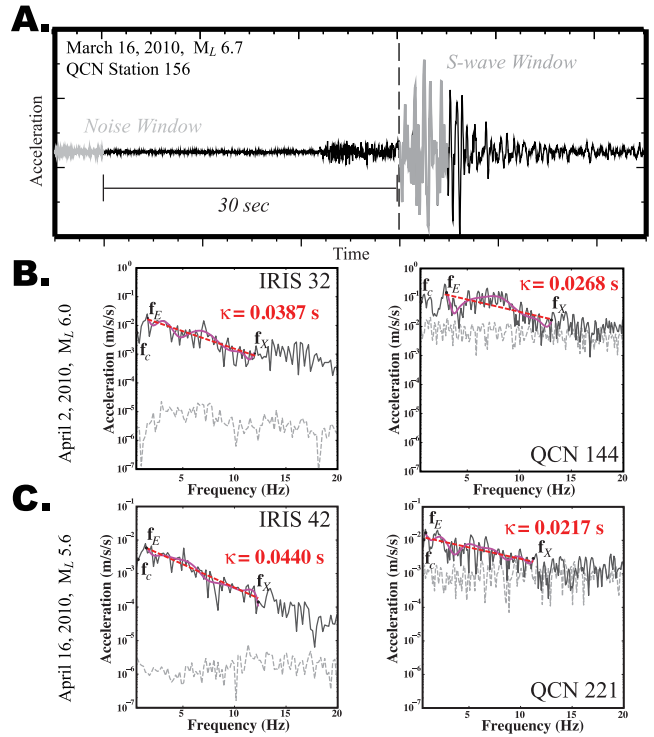
Figure 3. (a) Acceleration time-series record from QCN station 156 of the largest magnitude aftershock (M_L 6.7). Dashed black line represents manual pick of *S* wave. The 5-s noise (light grey) and *S*-wave (dark grey) windows are plotted in the frequency-domain to determine κ. (b) and (c) Examples of acceleration spectra for events recorded by stations located on the same geological unit; note that stations are not co-located. Purple line is the spline fit to spectrum over frequency band fit for κ (red dashed line). IRIS 32 and QCN 144 are classified as Sediment and IRIS 42 and QCN 221 are in the Hard Rock class for this study.

where λ is the slope of the line (Douglas *et al.* 2010). To limit the influence of source effects in the measurement of κ, the point of the initial linear downward trend in acceleration, f_E, should be above the corner frequency, f_c. We calculate the theoretical f_c for the event and verify that the f_E picks are above f_c; we identify f_E as the point at which the low-frequency, flat portion of the spectrum transitions to a linearly decaying spectrum in f versus log[$a(f)$] space. The point f_X is chosen such that it is before the *S*-wave spectrum meets the noise spectrum at higher frequencies. We use a lower SNR criterion (1.5) than the suggested ratio of 3 (Ktenidou *et al.* 2013) due to the higher noise level of the QCN instruments.

The f_E and f_X points are picked using an automated method adapted from Gentili & Franceschina (2011; Figs 3b and c). Due to the noisy characteristic of the QCN acceleration spectra, we use a least squares method to fit a spline to the spectrum between the f_E and f_X points and then linearly regress the spline interpolation to estimate κ for each record. We find that κ estimates on the north and east horizontal components have a median of 20.9 per cent difference for QCN records and 13.1 per cent difference for IRIS CHAMP stations. The QCN stations exhibit larger differences in κ estimates due to overall lower SNR and because the slope is estimated across narrower frequency bands. We find that f_E typically ranges from 1 to 13 Hz and f_X varies between 11–23 Hz for QCN and 1–20 Hz and 11–31 Hz, respectively, for IRIS CHAMP.

As we intend to combine networks for later analysis, we check that the κ estimates observed on the sensors are comparable by adding

QCN noise to the higher quality IRIS records. IRIS records were resampled and QCN-level instrument noise was added to the signal; we then re-estimated κ and compared the noise-added κ estimate to the original κ for that record. Due to the high QCN instrument noise, we ran both IRIS-scaled (multiplied by a factor of 1.25) and non-scaled (no multiplier applied) data through the automated κ picker. Scaled records are, in general, less than 1 per cent different between original and noise-added κ estimates and non-scaled are less than 5 per cent different. This suggests that the noisier QCN sensors provide reliable κ estimates and allows for the integration of the κ estimates from the two networks in later analysis.

For more robust estimates of κ at a single station location, multiple records for that station should be considered in the analysis. Here we only include stations that have reliable κ estimates for at least three earthquakes. The use of multiple earthquakes reduces bias from records that may be impacted by high corner frequencies or anomalous near-source effects as demonstrated in Kilb *et al.* (2012). Previous studies have shown that κ should be estimated over a wide frequency band, with bandwidths between 10 and 34 Hz (Parolai & Bindi 2004; Drouet *et al.* 2008); many studies have successfully used frequency bandwidths of 10 Hz, near the suggested lower limit (e.g. Anderson & Hough 1984; Castro *et al.* 2000). Thus, we require that κ estimates must be calculated over at least a 10 Hz band. Finally, κ estimates produced by the automated method are visually inspected for accuracy.

3.1 κ-Distance model

For the analysis, we use data from 40 stations (21 QCN RAMP and 19 IRIS CHAMP) and 39 unique earthquakes, for a total of 724 horizontal component records. Once κ is estimated from the spectra, the dependence on epicentral distance, r_{epi} and site conditions, z, can be developed using the model

$$\kappa(r_{epi}, z) = \kappa(r_{epi}) + \kappa_0^r(z), \tag{3}$$

where $\kappa(r_{epi}) = $ slope $\times r_{epi}$, the slope represents the dependence of κ with r_{epi} and describes the regional path attenuation; $\kappa_0^r(z)$ is a constant related to the near-surface attenuation (Anderson & Hough 1984). The κ model developed by Anderson & Hough (1984) simplifies the path into horizontal and vertical travelling ray paths, where the horizontally travelling path is reflected in the dependence of κ with r_{epi} and represents the regional attenuation and the vertically travelling wave path directly beneath the station is inferred to represent the site kappa, $\kappa_0^r(z)$. As such, we find the regional distance-dependence of κ using epicentral, rather than hypocentral, distance.

We use the regional dependence of κ with r_{epi} to find the site term, $\kappa_0^r(z)$, for each station. To determine the distance-independent ($r_{epi} = 0$) station-specific site term, $\kappa_0^r(z)$, we plot all κ observations for a station and fit the regional distance-dependent linear regression to those observations. Using eq. (3), we assume that the slope, or the dependence of κ with r_{epi}, is the same for all stations and find the intercept, $\kappa_0^r(z)$, by minimizing the sum of squared residuals between κ observations and the attenuation model at each station. This process yields the site term, $\kappa_0^r(z)$, for each station, which is thought to reflect the attenuation in the upper few kilometres and has been shown to be in fairly good agreement with V_{s30}, though there remains debate concerning the response of 'rock' sites that may have varying degrees of weathering and/or topographic effects (e.g. Atkinson 1996; Van Houtte *et al.* 2011; Laurendeau *et al.* 2013). Later, we compare the distance-independent site term at

each station, $\kappa_0^r(z)$, solved in eq. (3) to the magnitude–distance-independent site term at each station, $\kappa_0^{r,M}(z)$, using a multivariable inversion.

3.2 κ–distance, magnitude model

In addition to epicentral distance, we also consider whether κ is influenced by the magnitude of the source. To describe the κ observations in terms of both distance and magnitude, we perform a multivariable inversion to fit a surface to the data using a non-negative least squares approach, similar to the methods of Anderson & Lei (1994) and Fernández *et al.* (2010). We also include the near-surface site contribution, z, such that we solve

$$\kappa(r_{epi}, M_L, z) = \kappa(r_{epi}, M_L) + \kappa_0^{r,M}(z), \tag{4}$$

where $\kappa_0^{r,M}(z)$ is the magnitude- and distance-independent near-surface geological contribution to κ at each station. Eq. (4) can be written in matrix form as

$$
\begin{bmatrix}
C_{11}^1 & C_{12}^1 & \dots & C_{IJ}^1 10 \dots 0 \\
C_{11}^2 & C_{12}^2 & \dots & C_{IJ}^2 10 \dots 0 \\
 & & \vdots & \\
C_{11}^N & C_{12}^N & \dots & C_{IJ}^N 0 \dots 1 \\
W_{11}^1 & W_{12}^1 & \dots & W_{IJ}^1 0 \dots 0 \\
 & & \vdots & \\
W_{11}^M & W_{12}^M & \dots & W_{IJ}^M 0 \dots 0
\end{bmatrix}
\begin{bmatrix}
\kappa_{11} \\
\kappa_{12} \\
\vdots \\
\kappa_{IJ} \\
\kappa_{0,1} \\
\vdots \\
\kappa_{0,Z}
\end{bmatrix}
=
\begin{bmatrix}
D^1 \\
D^2 \\
\vdots \\
D^N \\
0 \\
0 \\
\vdots \\
0
\end{bmatrix}, \tag{5}
$$

where C_{IJ}^N is a series of interpolation functions solved for each data point, n,

$$C_{i,j}^n = \left(\frac{M_{k+1} - M}{M_{k+1} - M_k} \right) \left(\frac{R_{l+1} - R}{R_{l+1} - R_l} \right)$$

$$C_{i+1,j}^n = \left(\frac{M - M_k}{M_{k+1} - M_k} \right) \left(\frac{R_{l+1} - R}{R_{l+1} - R_l} \right)$$

$$C_{i,j+1}^n = \left(\frac{M_{k+1} - M}{M_{k+1} - M_k} \right) \left(\frac{R - R_l}{R_{l+1} - R_l} \right)$$

$$C_{i+1,j+1}^n = \left(\frac{M - M_k}{M_{k+1} - M_k} \right) \left(\frac{R - R_l}{R_{l+1} - R_l} \right). \tag{6}$$

For each distance, R and magnitude, M, associated with a κ observation, n, eq. (6) is calculated for intervals $R_l \leq R < R_{l+1}$ and $M_k \leq M < M_{k+1}$. Grid intervals were chosen using regularly spaced bins for each magnitude and distance class. For magnitude, we set $I = 6$ with bin-spacing 0.3 M_L, such that $M = 4.5, 4.8, 5.1, 5.4, 5.7$ and 6.0. For distance, we use $J = 5$ with bin-spacing 50 km, such that $R = 25, 75, 125, 175$ and 225 km. Imposing the grid reduced the data to 547 records (24 per cent reduction) on the north and east components, removing data outliers where too few observations left the solution underdetermined. After filling the sparse C-matrix with C_{IJ}^N solutions, we solve the inverse problem using the estimated κ values at all stations, D^N. κ_{IJ} are the interpolated values of κ at the nodal points of the $\kappa(R, M)$ grid. A station site term, $\kappa_{0,z}$, is included in the solution where Z is the number of stations where D^N are estimated. To solve for the station site term, we horizontally append the C-matrix with a sparse station matrix, in which a 1 is placed on the diagonal for the station where D^n is measured.

The $\kappa(r_{epi}, M_w, z)$ surface is smoothed using a weighting parameter chosen to limit oscillations and minimize solution roughness

Table 2. List of 39 events used in the final analysis. The average kappa for each event, known as κ_{event}, as well as κ_{event} distinguished by station geological class (e.g. $\kappa_{event,sediment}$) are included. Dashes represent limited or no data, meaning the event was either not recorded by stations of that geological class or recorded by only one station of that geological class.

Event	Latitude	Longitude	Depth	M_L	Number records	κ_{event} (s)	$\kappa_{event,sediment}$ (s)	$\kappa_{event,softrock}$ (s)	$\kappa_{event,hardrock}$ (s)
2010072031501	−36.685	−73.612	−15.0	5.9	14	0.026	0.0235 ± 0.0027	0.0297 ± 0.0073	0.0206 ± 0.0023
2010072031907	−36.679	−73.604	−30.3	5.3	12	0.024	0.0164 ± −	0.0306 ± 0.0076	0.0195 ± 0.0046
2010075022157	−36.471	−73.900	−25.0	6.7	17	0.037	0.0387 ± 0.0082	0.0371 ± 0.0071	0.0355 ± 0.0049
2010075030439	−36.491	−73.689	−21.2	6.1	11	0.035	0.0450 ± 0.0007	0.0380 ± 0.0070	0.0259 ± 0.0097
2010076190006	−36.754	−73.324	−44.2	5.2	8	0.019	0.0191 ± 0.0024	0.0153 ± 0.0039	0.0373 ± −
2010076225229	−36.896	−73.120	−35.0	4.8	9	0.016	0.0233 ± 0.0131	0.0093 ± 0.0010	0.0128 ± 0.0029
2010077015729	−36.511	−73.183	−28.1	5.5	14	0.029	0.0249 ± 0.0077	0.0293 ± 0.0082	0.0320 ± 0.0105
2010080152857	−36.349	−73.596	−21.5	4.7	5	0.023	− ± −	− ± −	0.0226 ± 0.0117
2010080183104	−36.358	−73.678	−10.5	5.9	10	0.023	0.0148 ± 0.0020	0.0259 ± 0.0067	0.0250 ± 0.0051
2010083000514	−37.176	−74.184	−19.0	5.0	3	0.038	− ± −	− ± −	0.0378 ± 0.0148
2010083113012	−36.542	−73.775	−28.1	5.1	4	0.031	− ± −	− ± −	0.0315 ± 0.0100
2010085124154	−36.604	−73.458	−20.4	4.7	11	0.028	0.0356 ± 0.0002	0.0282 ± 0.0081	0.0253 ± 0.0051
2010087213828	−35.364	−73.423	−27.8	5.9	11	0.036	0.0376 ± 0.0134	− ± −	0.0235 ± −
2010088030739	−37.203	−74.151	−18.8	4.9	15	0.040	0.0423 ± 0.0101	− ± −	0.0358 ± 0.0089
2010092103824	−36.700	−73.614	−26.7	4.9	18	0.028	0.0275 ± 0.0113	0.0233 ± 0.0034	0.0307 ± 0.0064
2010092183258	−37.283	−72.944	−58.9	4.8	18	0.018	0.0199 ± 0.0085	0.0122 ± −	0.0150 ± 0.0078
2010092193410	−36.118	−72.898	−29.0	5.5	16	0.025	0.0240 ± 0.0112	− ± −	0.0272 ± 0.0126
2010092225807	−36.201	−73.211	−27.9	6.0	32	0.024	0.0244 ± 0.0102	0.0273 ± 0.0030	0.0225 ± 0.0094
2010093015057	−36.979	−72.187	−05.0	4.4	16	0.027	0.0281 ± 0.0074	0.0176 ± −	0.0264 ± 0.0087
2010093021239	−36.280	−73.178	−25.7	5.1	9	0.020	0.0185 ± 0.0073	0.0252 ± 0.0049	0.0203 ± 0.0179
2010093084121	−36.705	−73.298	−23.4	4.7	15	0.022	0.0207 ± 0.0094	0.0262 ± 0.0072	0.0163 ± 0.0005
2010097111349	−36.478	−73.270	−15.4	4.4	29	0.029	0.0287 ± 0.0134	− ± −	0.0300 ± 0.0046
2010097175039	−37.127	−73.254	−18.7	4.9	37	0.027	0.0273 ± 0.0124	0.0252 ± 0.0150	0.0256 ± 0.0134
2010098222114	−36.675	−73.610	−21.8	4.6	32	0.035	0.0370 ± 0.0102	0.0228 ± 0.0073	0.0364 ± 0.0062
2010105121246	−36.601	−72.862	−37.6	4.7	32	0.024	0.0255 ± 0.0118	− ± −	0.0231 ± 0.0094
2010106223827	−37.097	−74.677	−25.0	5.1	29	0.040	0.0407 ± 0.0097	− ± −	0.0394 ± 0.0100
2010106224133	−37.579	−74.151	−28.1	5.2	15	0.038	0.0414 ± 0.0064	0.0058 ± −	0.0379 ± 0.0127
2010106231536	−37.604	−74.658	−20.0	5.6	37	0.038	0.0409 ± 0.0043	0.0268 ± −	0.0355 ± 0.0098
2010116084429	−37.413	−73.186	−56.2	4.8	27	0.028	0.0276 ± 0.0097	0.0146 ± −	0.0294 ± 0.0109
2010119134013	−36.854	−73.183	−33.9	5.2	20	0.024	0.0274 ± 0.0066	0.0345 ± 0.0106	0.0164 ± 0.0069
2010128215253	−36.113	−73.637	−31.6	5.0	24	0.037	0.0416 ± 0.0122	− ± −	0.0302 ± 0.0128
2010129134300	−36.687	−74.558	−45.0	4.6	22	0.027	0.0268 ± 0.0123	− ± −	0.0258 ± 0.0094
2010137211643	−36.686	−73.267	−34.7	5.1	32	0.025	0.0282 ± 0.0117	0.0261 ± 0.0063	0.0203 ± 0.0109
2010144191217	−35.769	−72.856	−31.4	5.4	25	0.029	0.0313 ± 0.0085	− ± −	0.0235 ± 0.0039
2010144235737	−36.342	−73.601	−26.9	5.4	3	0.032	− ± −	0.0339 ± 0.0058	0.0268 ± −
2010149191808	−36.848	−73.730	−09.6	4.7	34	0.034	0.0353 ± 0.0107	− ± −	0.0327 ± 0.0114
2010152160529	−36.886	−73.543	−25.3	5.7	32	0.039	0.0412 ± 0.0106	0.0342 ± 0.0000	0.0380 ± 0.0080
2010175132409	−37.115	−73.975	−22.8	5.2	6	0.031	0.0381 ± 0.0042	− ± −	0.0180 ± 0.0003
2010180124914	−36.358	−73.885	−19.2	4.8	9	0.029	0.0291 ± 0.0052	0.0280 ± 0.0000	0.0296 ± 0.0001

and misfit. To minimize oscillations in the surface, we smooth the solution by imposing the 2-D second derivative of κ_{ij} with respect to both distance and magnitude (e.g. Anderson & Lei 1994; Jónsson *et al.* 2002). The weighting scheme, W_{IJ}^M, for each interval of the grid can be solved using

$$W_{ij}^m = w \left[\frac{c_{i-1,j} - 2c_{i,j} + c_{i+1,j}}{(\Delta l_M)^2} + \frac{c_{i,j-1} - 2c_{i,j} + c_{i,j+1}}{(\Delta l_R)^2} \right], \quad (7)$$

where $M = I \times J$, $c_{i,j}$ is an individual grid cell, $\Delta l_{M,R}$ are the distances between grid nodes of magnitude and hypocentral distance and w is the weighting factor. We used various weighting factors ranging from 0.1 to 2.0 for weak to strong smoothing, respectively, where lower weights fit the κ_{ij} solution better and higher weights favour a smooth surface.

4 RESULTS

A total of 39 earthquakes recorded by 21 QCN RAMP stations and 19 IRIS CHAMP stations were used in the final analysis. For QCN RAMP data, the average κ values at a station, κ_{ave}, range from

a minimum of 0.0108 to a maximum of 0.0379 s, with an overall average of 0.0256 ± 0.0069 s (Table 2). IRIS CHAMP stations have κ_{ave} values between 0.0219 and 0.0420 s with an average of 0.0315 ± 0.0064 s. The κ estimates recorded on the low-resolution QCN RAMP stations are in agreement with the higher-resolution IRIS CHAMP stations, thus, we combine the two data sets in the analysis below.

4.1 Influence of epicentral distance on κ

To investigate the correlation of κ values with source-to-station distance, we plot κ estimated on both horizontal components versus epicentral distance. As shown in Fig. 4, κ increases with increasing epicentral distance, for example, positive slope in the $\kappa(r_{epi})$ equation; although, there is significant scatter in the κ values across the distances observed ($r_{epi} \leq 250$ km). By fitting a linear slope to the κ points using a least squares approach, we find the slope to be 5.991 $\times 10^{-5} \pm 7.209 \times 10^{-6}$ s km^{-1}. While there is no physical basis for assuming a linear dependence on attenuation with distance (e.g. Anderson 1991), using a polynomial does not significantly increase
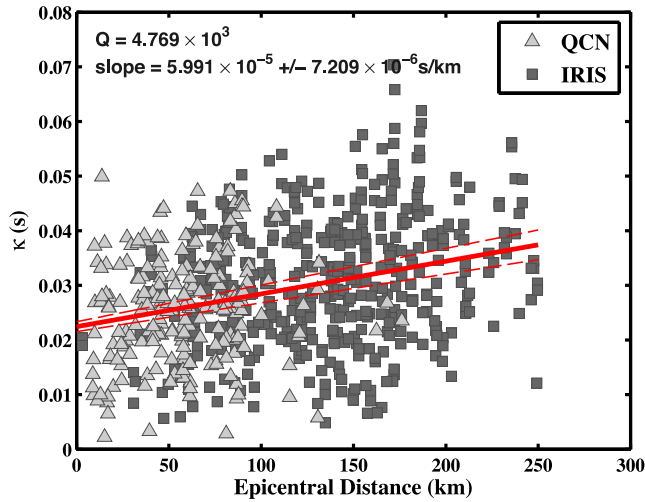
Figure 4. (a) κ estimates plotted versus epicentral distance. The dependence of κ with r_{epi}, or the slope, of the linear regression describes the attenuation along the horizontal ray path. The slope and standard error in slope are $5.991 \times 10^{-5} \pm 7.209 \times 10^{-6}$ s km^{-1} and are shown as solid and dashed lines, respectively.

the goodness of fit. The *R*-squared value remains below 10 per cent for complex regressions and without knowledge of the *Q*-structure in the region we do not believe that a higher order fit is justified.

Kappa values versus epicentral distance for a subset of stations are plotted in Fig. 5 and $\kappa_0^r(z)$ for all station are given in Table 2. The κ values at some stations (e.g. Station 108, 125) show a relatively good fit to the $\kappa_0^r(z)$ model, while others show larger scatter (e.g. Station 28, 156). The estimates of $\kappa_0^r(z)$ range from 0.00590 to 0.0335 s, with a mean of 0.0223 s and standard errors of 0.00686 s, on average.

4.2 Influence of epicentral distance and magnitude on κ

To determine if a correlation exists between κ and event size, we plot κ versus event magnitude. We fit a linear regression to the points and see a positive correlation between κ and magnitude with a slope of $2.444 \times 10^{-3} \pm 8.208 \times 10^{-4}$ s/M_L (Fig. 6). Again, we use a linear regression as the scatter in the data do not warrant a higher polynomial fit. To ensure this slope is not controlled by a relatively small number of κ measurements at higher magnitudes, we removed the measurements from the M_L 6.7 event. Though there is large scatter in the κ observations for a given magnitude, we still find a similar slope with the M_L 6.7 records removed.

Having established that κ measurements in Bío Bío appear to be influenced by both epicentral distance and source magnitude, we examine the relative importance of these effects by performing a multivariable inversion. Fig. 7 exhibits two possible solutions of the magnitude–distance inversion (eq. 4) found by applying different levels of smoothing. We show the surfaces for smoothing weights of $w = 0.2$ and $w = 1$ in both 2-D and 3-D views. The solution of the lower smoothing weight is highly peaked and likely reflects the large uncertainty in the data rather than providing a plausible relationship between κ, magnitude and epicentral distance. We apply higher weighting until the nodal points stop oscillating and become stable, which occurs around $w = 1$ where surface roughness is appropriately minimized without significant misfit to the data. Higher weight ($w = 2$) produces an overly smooth surface that is a poorer fit to the data. Note that the grid used does not include outliers at far

distances and large magnitudes (Fig. 2, dashed lines). The inverse solution shows a gradual increase in κ with both increasing distance and magnitude. These results further support the observation that κ is influenced by both the distance and magnitude of the recorded events. There are some small amplitude oscillations in the surface in addition to the linear trends, but further interpretations are not warranted due to the large scatter in the individual κ measurements.

Having shown that both source and path are influential to κ, we also solve for the station site term, $\kappa_0^{r,M}(z)$, in the matrix inversion (eq. 4). The inversion solution arguably provides a more robust estimate of the station term than eq. (3) as it is less affected by the station recording only a limited magnitude or source–receiver distance range. $\kappa_0^{r,M}(z)$ values for each station are given in Table 2 and mapped in Fig. 8. The estimates of $\kappa_0^{r,M}(z)$ range from 0.00582 to 0.0321 s with a mean of 0.0209 s. For most stations the $\kappa_0^{r,M}(z)$ value is smaller than the $\kappa_0^r(z)$ solution (Figs 8c and d), highlighting the combined influence of distance and source. A more thorough explanation of the differences in the station terms derived across the methods is addressed in Section 5.

4.3 κ_0-influence of site geology

We investigate whether the observed average kappa, κ_{ave}, and the site terms, $\kappa_0^r(z)$ and $\kappa_0^{r,M}(z)$, are correlated to the mapped, near-surface geology at a station. We use a geological map of Chile published by the Chilean National Service of Mining and Geology (Servicio Nacional de Geologia y Mineria 1982). It is important to note that this geological map is fairly low resolution and the depth of the sediments, which has been shown to influence κ, is unknown. However, no higher resolution geological maps covering the entire study area are available. We reclassify the map into three geological classes: Sediment, Soft Rock and Hard Rock (Table 2, Fig. 8). The Sediment group is characterized by mapped Quaternary Fluvial (*Q*) lithology; Soft Rock by Tertiary sedimentary rocks (Te) including sandstones, shales, siltstones and conglomerates; and Hard Rock by Palaeozoic and Tertiary plutonic rocks (Pzg, Tg). There are 16 stations on Sediment, 8 stations on Soft Rock and 16 stations on Hard Rock.

We use the mapped geological class to compare the influence of the site material on $\kappa_0^r(z)$, the original site term model from Anderson & Hough (1984) found by extrapolating the distance-dependent relationship to $r_{epi} = 0$ (eq. 3, Fig. 8c) and $\kappa_0^{r,M}(z)$, the site term solved for in eq. (4) that accounts for both the magnitude of the events and the source-to-site distance (Fig. 8d). In the eastern part of the study area there appears to be some indication of a spatial correlation in the site kappa measurements and geological material as $\kappa_0^r(z)$ and $\kappa_0^{r,M}(z)$ values are generally larger for stations located on sediment and smaller for stations located on Hard Rock. For instance, stations 30, 32 and 35 have higher than average $\kappa_0^r(z)$ and $\kappa_0^{r,M}(z)$ values (0.028 and 0.0305 s, 0.0321 and 0.0315, 0.0244 and 0.0236 s, respectively) and are located on a large sediment-classified valley running NE–SW through our study area. However, this correlation is less apparent to the west, which has more variable geomorphology (hilly basement rock cut by low-lying sediment-filled riverine systems). And, when considering the entire dataset, we find no correlation between geological class and $\kappa_0^r(z)$ or $\kappa_0^{r,M}(z)$. The sites on Sediment have a mean κ_0^r and $\kappa_0^{r,M}(z)$ values of 0.0217 ± 0.0069 s and 0.0200 ± 0.0069 s, respectively and sites on Hard Rock that have a mean κ_0^r and $\kappa_0^{r,M}(z)$ values of 0.0223 ± 0.0080 s and 0.0219 ± 0.0083 s, respectively. Note that the error bars overlap for the mean values of κ_0^r and $\kappa_0^{r,M}$ for the sediment and rock classes.
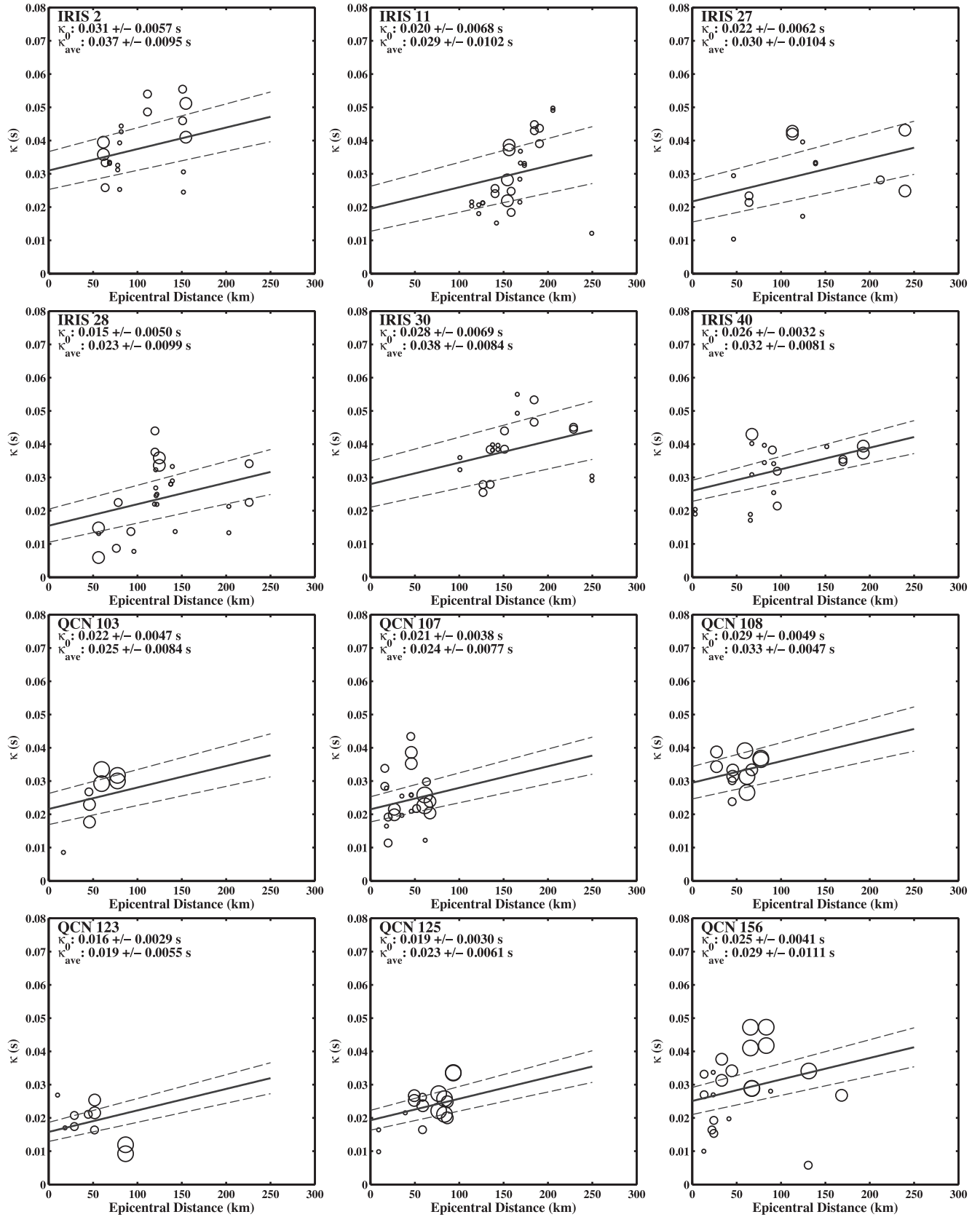
Figure 5. Plots showing the site term, $\kappa_0^r(z)$ (intercept), for a subset of stations. The slope represents the regional attenuation and is held fixed at 5.991×10^{-5} $\pm\ 7.209 \times 10^{-6}$ s km^{-1}; the localized, vertical attenuation is represented by the intercept, $\kappa_0^r(z)$, and is allowed to vary at each station. Markers are scaled by event magnitude.
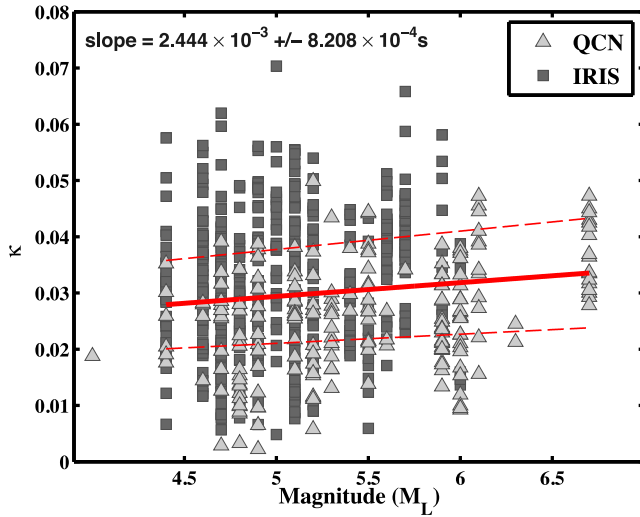
Figure 6. κ Estimates for both networks are plotted versus magnitude. Slope and standard error in slope are $2.444 \times 10^{-3} \pm 8.208 \times 10^{-4}$ s and shown as solid and dashed lines, respectively.

Assuming that κ_{ave} represents a combination of the source–receiver distance, source magnitude and geology, we can estimate the relative influence of source–receiver path and source magnitude by comparing κ_{ave}, $\kappa_0^r(z)$ and $\kappa_0^{r,M}(z)$. We find that merely a third (33 per cent) of the stations display a significant difference between κ_{ave} and $\kappa_0^r(z)$, for example the standard deviation of the κ_{ave} does not overlap the $\kappa_0^r(z)$ value, signifying that distance has only a minor influence on κ measurements. When we account for the combined effect of distance and magnitude, 44 per cent of the stations show significantly different values, suggesting that source size also contributes to the measured κ. The effect of geology on measured κ is more difficult to quantify due to the limited geological data available. However, the lack of a positive correlation of $\kappa_0^r(z)$ and $\kappa_0^{r,M}(z)$ values with the mapped geology suggests the surficial geology may not strongly influence kappa in our study area.

4.4 Influence of source location and depth on κ

Accounting for epicentral distance, magnitude and near-surface geology does not appear to fully explain the observed scatter in κ, so we briefly examine whether κ is influenced by source location or depth. Laterally heterogeneous attenuation near the earthquake source or azimuthally-variable regional attenuation may result in more scattered κ measurements (e.g. Castro *et al.* 2000; Fernández *et al.* 2010; Gentili & Franceschina 2011). To investigate, we first plot the average κ for each event, known as κ_{event}, on the event location (e.g. Purvance & Anderson 2003). Fig. 9(a) shows that while κ_{event} varies for individual events, there does not appear to be any spatial correlation in κ_{event}. We also plot κ estimates grouped by azimuth to determine if κ is azimuth dependent. Fig. 9(b) shows κ versus epicentral distance for six azimuth bins. No clear shift in κ values with azimuth is apparent. Although, as most events occurred to the west of the study area, we have limited azimuthal coverage with which to determine if a true directional partiality exists.

We also investigate whether the event depth influences the slope in the $\kappa(r_{epi})$ equation. One might expect weaker dependence, or a lower slope, for events with greater source depths since the horizontally traveling ray paths of deep earthquakes primarily sample the less attenuating, deeper crust. Conversely, for shallow events a stronger dependence, or a steeper slope, is expected as the ray paths

sample the more attenuating upper crust, which could account for some of the variability in κ estimates (e.g. Anderson & Hough 1984). The earthquakes used in this study have hypocentral depths ranging from 5 to 59 km (Fig. 10). Based on seismic tomographic inversions of the region suggesting typical crustal depths of 20 km (Hicks *et al.* 2012), we reclassify the κ observations into shallow (depth $\leq$ 20 km) and deep (20 > depth $\leq$ 40) event bins. We plot estimated κ values for events within these depth groups and estimate the dependence of κ with r_{epi} by fitting a linear slope to each set of points. For the shallow event bin we find a slope of $7.677 \times 10^{-5} \pm 1.209 \times 10^{-5}$ s km^{-1} and for the deeper event bin we find a slope of $5.590 \times 10^{-5} \pm 9.809 \times 10^{-6}$ s km^{-1}. Thus, the slopes for shallow and deep events are not significantly different and are unlikely to contribute to the observed scatter in κ.

5 DISCUSSION

For the over 700 records analysed, we find an average κ of 0.0295 s in central Chile, which is comparable to κ obtained in analogous active tectonic regions, including central-eastern Italy (Castro *et al.* 1990), western Mexico (Purvance & Anderson 2003) and Greece (Ktenidou *et al.* 2013). There is good agreement between the κ estimates determined here with respect to tectonic regime; the κ values are more similar to those found in tectonically active western North America (WNA, 0.040 s) than stable eastern North America (ENA, 0.006 s; Anderson & Hough 1984 and Toro *et al.* 1997, respectively).

We find that κ is dependent on distance, such that κ increases with source–receiver epicentral distance, as reported in previous studies. The κ-distance slope is $5.991 \times 10^{-5} \pm 7.209 \times 10^{-6}$ s km^{-1}, which corresponds to a frequency-independent Q of 4769. This slope is shallow compared to the κ-derived regional attenuation from studies of other regions; for example, Van Houtte *et al.* (2011), Douglas *et al.* (2010) and Jo & Baag (2007) find the slope to be an order of magnitude higher for crustal events in Japan (2.15×10^{-4} s km^{-1}), France (1.80×10^{-4} s km^{-1}) and South Korea (1.388×10^{-4} s km^{-1}), respectively. This Q value is large compared to other studies, such as observed by Edwards *et al.* (2011) in Switzerland (1216) and Gentili & Franceschina (2011) in Solvenia and northeastern Italy (2140) (refer to Edwards *et al.* (2011) for a discussion of Q derived from the κ-distance slope). Yet it has been noted that portions of the Chilean subduction zone are characterized by higher than average seismic velocity and Q ($\leq$ 2000) in comparison to other subduction zones (e.g. Myers *et al.* 1998; Schurr *et al.* 2003). Additionally, some recent studies have suggested that κ measurements are not sensitive to the regional path attenuation in certain regions (e.g. Purvance & Anderson 2003; Kilb *et al.* 2012), the scatter within the κ measurements obscures the path influence (e.g. Rovelli *et al.* 1988), or the trend is variable by distance interval (e.g. Fernández *et al.* 2010).

In addition to path distance, the results of our analysis indicate that κ is influenced by the magnitude of the source. Previous studies have reported mixed outcomes for the relationship between κ and magnitude. For example, Jo & Baag (2007) and Fernández *et al.* (2010) examine smaller magnitude earthquakes ($M \leq 4.1$) and found little to no relationship between source magnitude and κ. Van Houtte *et al.* (2011) and Gentili & Franceschina (2011) also report no obvious trend between magnitude and κ in Japan ($4.0 \leq M_w \leq 7.3$) and in Solvenia and northeastern Italy ($3.0 \leq M_w \leq 5.7$). However, Tsai & Chen (2000) in Taiwan ($4.3 \leq M_L \leq 6.5$), Atkinson (1996) in Canada ($3.6 \leq M_w \leq 4.0$), Castro *et al.* (2000)
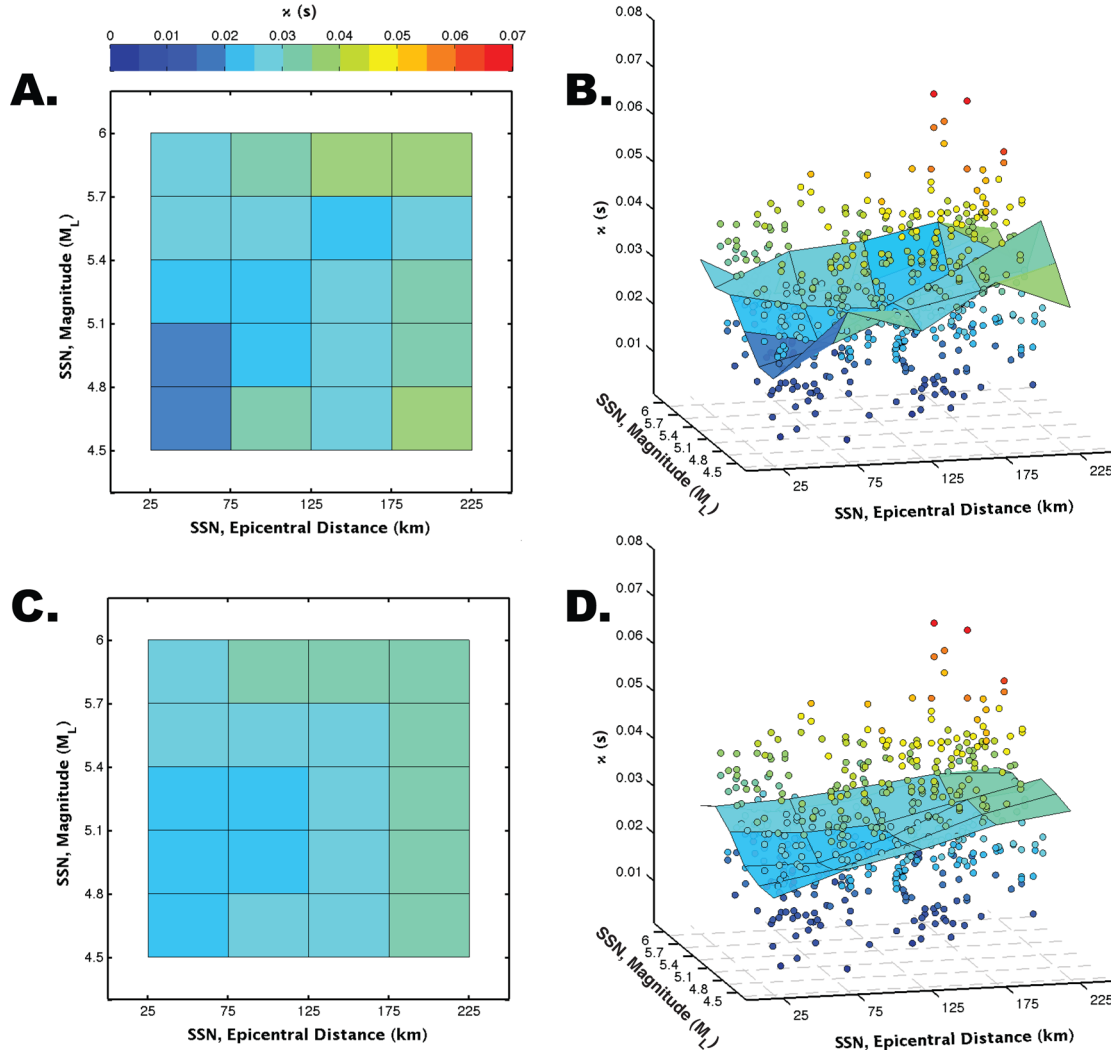
Figure 7. Surface solutions to eq. (4) inversion for κ as a function of distance and magnitude plotted in 2-D [(a)–(b)] and 3-D [(c)–(d)]. Panels (a) and (b) use a smoothing weight of $w = 0.2$ and (c) and (d) use a smoothing weight of $w = 1$. κ Observations are plotted as points in (b) and (d). Colourbar shown in (a) applies to κ points and κ surface solution for (a)–(d).

in central Italy ($2.1 \le M_L \le 4.1$) and Kilb *et al.* (2012) in California ($0.5 \le M_L \le 5.2$) observe an influence of source properties on κ measurements. Particularly, Purvance & Anderson (2003) find κ and magnitude to be correlated for moderate to large events ($5.1 \le M_w \le 8.0$). We also observe an increase in κ with magnitude and the inversion solution shows that even with the removal of large magnitude outliers (records of the M_L 6.7 aftershock, discussed in Section 4.2) there still exists a positive correlation between κ and magnitude. Purvance & Anderson (2003) also note that the influence of source magnitude in κ estimates could be due to differences in near-source material properties, such that rough faults may produce more high-frequency energy or bimaterial faults may produce varying high-frequency radiation patterns (Harris & Day 1997; Anderson *et al.* 2002). As shown in Figs 1 and 9, there is no apparent spatial correlation in κ_{event} that might suggest the near-source material properties influence κ. However, it is possible that large events rupture the main plate interface while smaller events occur on secondary faults with different material properties; this may explain the correlation between κ and magnitude. Another possible explanation that does not require a near-source influence

is nonlinear behaviour of geological materials for higher magnitude earthquakes. However, the recorded accelerations at all sites were relatively low suggesting nonlinear response is less likely. Thus, the underlying physical mechanism resulting in a correlation between κ and magnitude remains difficult to infer.

Most importantly in the investigation of κ for engineering seismology purposes is characterizing the extent to which the site kappa, $\kappa_0(z)$, correlates to the near-surface geology. $\kappa_0(z)$ values are highly region dependent, but rock sites typically have $\kappa_0(z)$ less than 0.01 s and sediment sites have $\kappa_0(z)$ above 0.02 s [see Van Houtte *et al.* 2011 and Ktenidou *et al.* 2014 for compilation of $\kappa_0(z)$ and V_{s30}]. We used two methods to extract the site term, $\kappa_0(z)$, from the κ measured from the spectrum—(1) characterizing the vertical distance-dependence beneath the station (eq. 3) yielding $\kappa_0^r(z)$ and (2) accounting for the effects of both distance and source magnitude simultaneously (eq. 4) giving $\kappa_0^{r,M}(z)$. The inversion solution (eq. 4) is likely a more robust estimate of the site attenuation as the inversion should reduce the effect of individual measurement errors and station recording bias. For example, on average, the QCN stations are biased to recording larger earthquakes at shorter
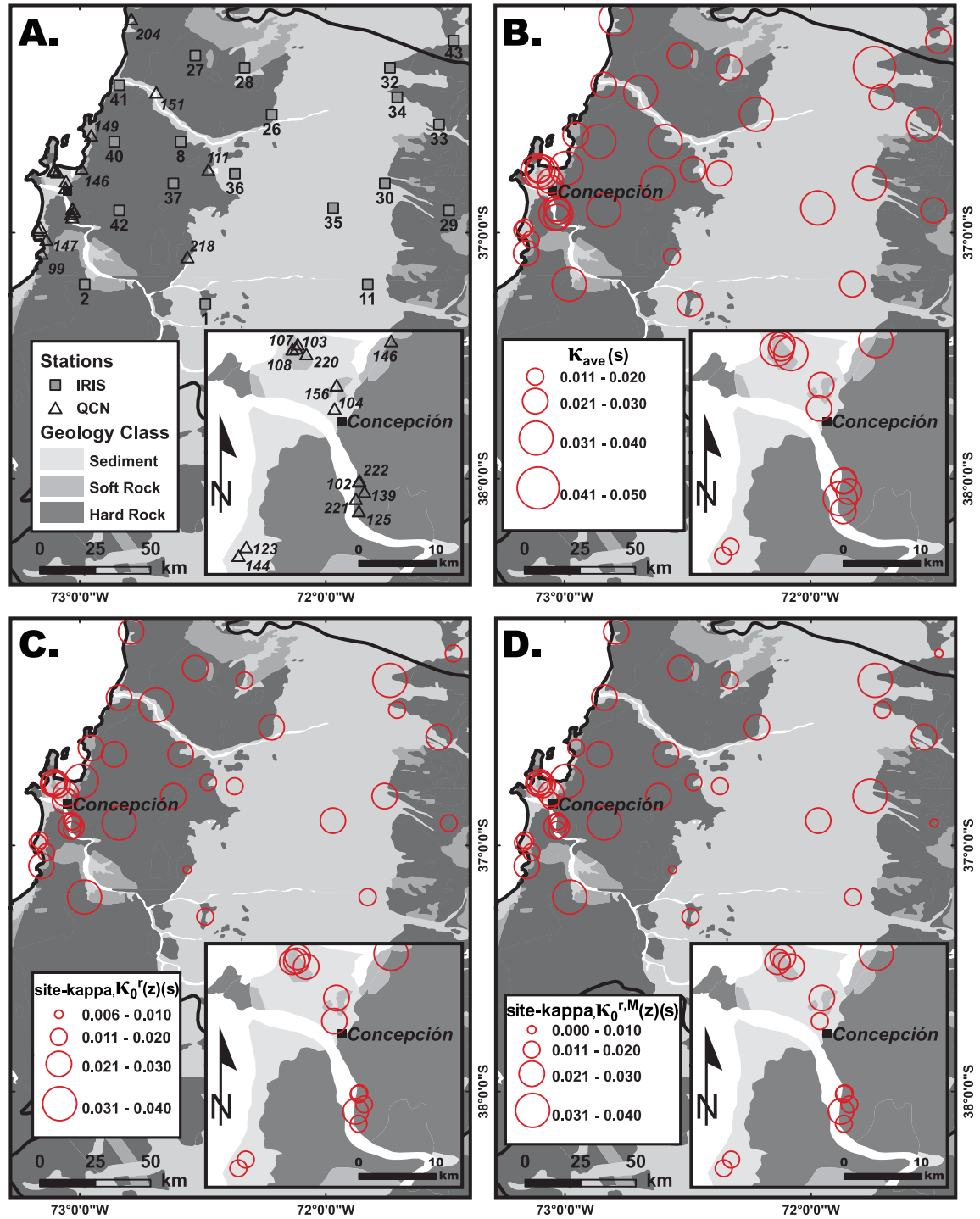
Figure 8. (a) Map of geological classes used in study (b) average κ per station, κ_{ave} (c) Map of distance-determined site term, $\kappa_0^r(z)$, solved in eq. (3). (d) Map of magnitude-distance-determined site term, $\kappa_0^{r,M}(z)$, solved in eq. (4). Location of regional capital, Concepción, plotted as a square.

source–receiver ranges than the IRIS stations because the sensors are lower resolution (Table 1).

Surprisingly, there is no apparent influence from the mapped geological material on the measured κ (Fig. 8). After accounting for path attenuation, κ_0^r, and combined distance and source magnitude, $\kappa_0^{r,M}$, we find the Hard Rock class has larger average κ_0^r and $\kappa_0^{r,M}$ values than the Sediment class; however, the error bars overlap suggesting this result is not significant. We note that 75 per cent of the

stations (30 of 40) are within 1 km and 85 per cent are within 5 km of a lithologic boundary, which may obscure any relationship between site geology and κ_0. Stations near mapped lithologic boundaries, particularly sites on thin sediment layers on top of Hard Rock, are likely to have intermediary $\kappa_0(z)$ measurements.

It is important to reiterate that the interpretation of $\kappa_0(z)$-geology results are based solely on the surficial geological map and the lithologic classification scheme used. This can be problematic in accu-
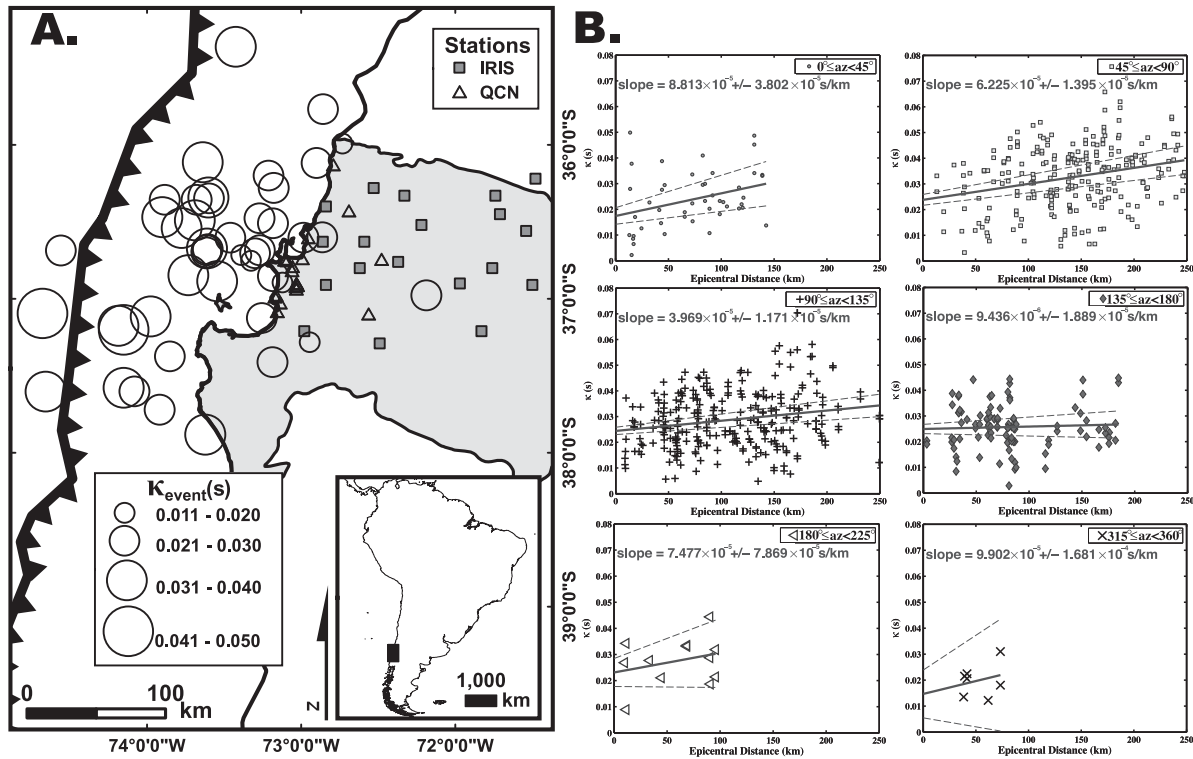
Figure 9. (a) Map of κ_{event}, or the average κ for each event as recorded at many stations. (b) κ for each event binned according to source-to-station azimuth and plotted by epicentral distance. Slope and standard error in slope shown as solid and dashed lines, respectively.

rately characterizing the site-influence of κ estimates; for example, lithologic units can encompass multiple rock types or one rock type of variable composition. The Hard Rock class used in this study includes both Palaeozoic and Tertiary plutonic rocks (Pzg and Tg, respectively). The difference in age of the rocks implies that over longer time intervals weathering processes could compromise the structure and competency of the rock yielding contrasting κ estimates between the younger and older rocks (as shown in Fernández *et al.* 2010). Here, one station (IRIS CHAMP 29) is located on a Tertiary plutonic rock unit, Tg, which accounts for 14 per cent of the Hard Rock class κ observations, and has an average κ_{ave} of 0.0219 ± 0.0102 s. The remaining 16 stations in the Hard Rock class are located on a Palaeozoic plutonic rock unit, Pzg, with a κ_{ave} of 0.0290 ± 0.0080 s. As the uncertainty in Tg and Pzg κ_{ave} values overlap, we feel it is acceptable to include these two plutonic units in a singular Hard Rock class; however, more data might help us to conclude that the younger rock is less (or more) attenuating.

Another interpretation of these results might be that the lithologic properties here are too similar to be differentiated by the κ measurement, for example, the behaviour of weathered bedrock ('Hard Rock') may be analogous to consolidated sediment ('firm-soil' or 'stiff-soil'). A better proxy for site geology would be to use something similar to the NEHRP site classification scheme (e.g. FEMA 1997) or, similarly, the measured shear wave velocity of the local geological material, such as V_{s30}, but to our knowledge systematic measurements of V_{s30} do not exist at the sites considered. This is a particularly critical point as previous studies have shown that there is significant variation in the definition and response of rock sites (e.g. Douglas *et al.* 2010; Van Houtte *et al.* 2011).

The results suggest that the source–receiver distance primarily influences the measured κ, with additional, smaller contributions from source size and surficial geology. Overall, we measure a rel-

atively small range in κ_{ave}, 0.0108–0.0420 s, for a wide range of path distances, source magnitudes and site geology, which suggests the influence of any one of these effects is limited. The difference between κ_{ave} and $\kappa_0^r(z)$ yields the relative contribution of path while the difference in κ_{ave} and $\kappa_0^{r,M}(z)$ gives the contribution of both path and magnitude. We find that κ_{ave} is similar to $\kappa_0^r(z)$ at a majority of stations (27, or 68 per cent, of the stations) suggesting the path influence is present; but, as the slope is shallow, the influence on measured κ is minor. We find that κ_{ave} is similar to $\kappa_0^{r,M}(z)$ at over half of the stations (22, or 56 per cent) suggesting that source magnitude does have some influence and that the combined effects of distance and source properties on the measured κ are greater than distance alone. These results are interesting, as one would expect that (1) in a crustally complex, active subduction zone the regional attenuation would be large (for example, see Van Houtte *et al.* 2011) and (2) source magnitude should have low to no effect as κ is measured above the corner frequency. However, our results are not anomalous; Purvance & Anderson (2003) also observed an influence from the source size and did not see a strong path influence in the Mexico subduction thrust. Additionally, Rovelli *et al.* (1988) noted only slight dependence in path length in central Italy and remarked that observed fluctuations in κ, both for a single event recorded at multiple stations and for many events covering a range of magnitudes recorded at one station, combined with variable geomorphology make trends difficult to discern. Conflicting attributions to κ across many studies suggests that spectral behaviour can vary across tectonic regions and event catalogues, thus we feel that investigations of κ should be undertaken on a region-by-region basis with careful consideration of confounding factors.

Even after accounting for epicentral distance, magnitude and surficial geology, there is still significant scatter in the data. We investigated whether there were additional source and path effects
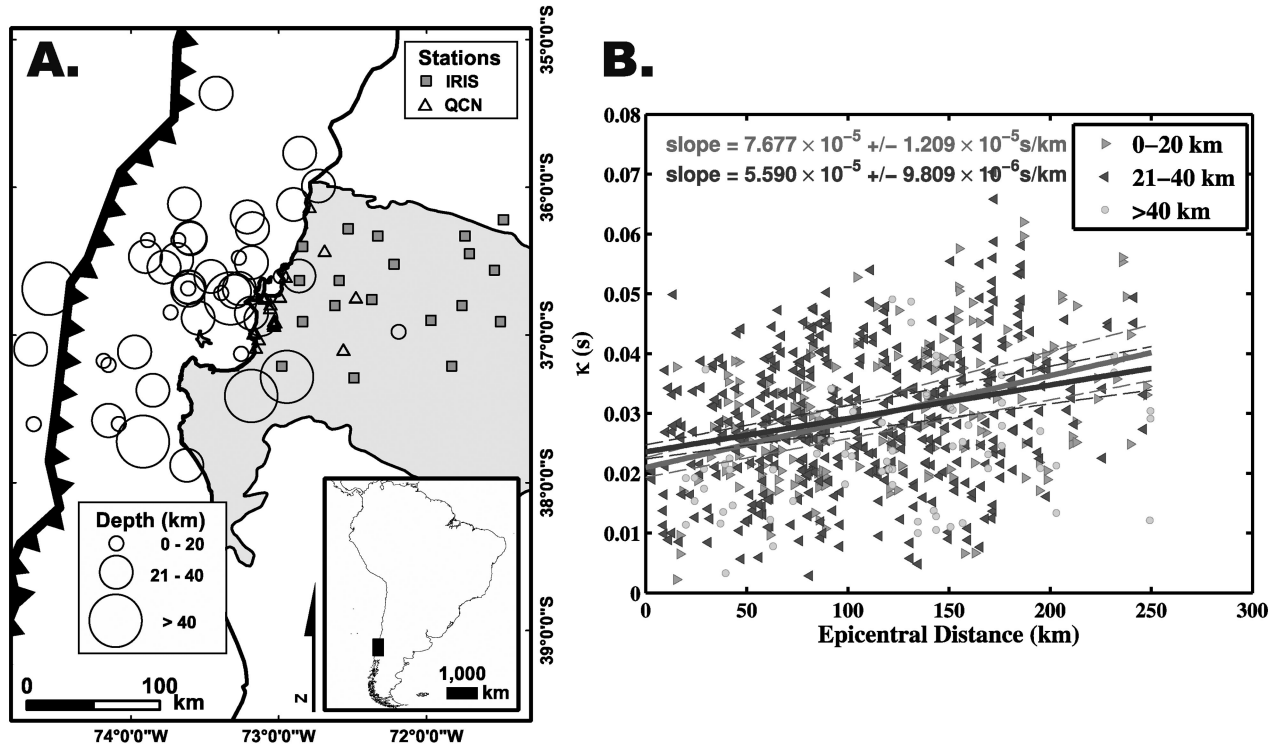
Figure 10. (a) Distribution of events scaled by hypocentre depth. (b) κ Measurements grouped into event depth bins and plotted by distance. Depth groups are linearly regressed to quantify the path attenuation for shallow (right-directed triangle) and deep (left-directed triangle) events. The dependence of κ with r_{epi}, or the slope, of the two depth bins, 0–20 km depth (light grey) and 21–40 km depth (dark grey), are shown as solid lines and the standard error in the slopes as dashed lines. Events deeper than 40 km (circles) are not fitted due to the limited number of observations.

due to event depth and/or directional dependence (Figs 9 and 10); yet we did not find any correlation between source depth, source location, or source-to-site azimuth and κ. Thus, the variability in κ values is likely due to a combination of these effects plus the inherent uncertainty in the measurement of κ.

6 CONCLUSION

We determined that κ, the high-frequency spectral decay parameter, in central Chile has an average value of 0.0295 s, which is comparable to κ obtained in analogous active tectonic regions. We find that κ is controlled primarily by the source–receiver distance, and to a lesser extent by source magnitude and, possibly, local site geology. Thus, while our study represents an important step toward measuring and investigating κ in Bío Bío, more data is needed to fully understand the scatter in κ measurements. For example, a regional velocity model, V_{s30} measurements at each site, and/or independent estimates of Q would help to further elucidate the results obtained here. Additionally, comparisons of κ measurements in different regions are difficult as different methods are used and different types of κ are reported [e.g. Original-kappa, AH-kappa, Displacement-kappa, Acceleration-kappa and Fixed-kappa (Kilb *et al.* 2012); also see Ktenidou *et al.* 2013 and 2014 for suggested data processing, analysis guidelines and nomenclature]. A method that simultaneously determines source, path and site terms such as the spectral fitting method (e.g. Kilb *et al.*'s (2012) Fixed-kappa) may be preferred. However, available datasets are often not sufficient for this method (as is the case in this study), since many recordings of an individual event by multiple stations are needed. Thus, in the future

consistent, and widely applicable, methods for estimating κ should be established providing more comparable sets of κ measurements.

We also show that lower-resolution MEMS sensors provide similar estimates of κ as high-quality, broadband seismometers. The ability to install 100 QCN sensors rapidly in a dense and low-cost deployment allowed for more recorded aftershocks, most notably the large M_L 6.7 aftershock, than the IRIS CHAMP deployment during the early aftershock period. However, it is important to note that the QCN data are subject to issues associated with placement in a building (e.g. availability of computer and internet for installation), high instrument noise, and coupling to the ground (e.g. non-free field recording). To date, the sensors have primarily been used for rapid event detection (e.g. Chung *et al.* 2011, 2014; Lawrence *et al.* 2014), but as shown here may also provide valuable contributions to attenuation and site response studies by providing spatially dense data. Newer, higher resolution QCN sensors (16-bit) have been developed since this study, which yield a lower noise threshold and provide improved data quality for future studies.

REFERENCES

Akkar, S., Douglas, J., Alessandro, C.Di., Campbell, K., Somerville, P., Cotton, F., Silva, W. & Baker, J., 2012. Defining a consistent strategy to model ground-motion parameters for the GEM-PEER Global GMPEs project, in *Proceedings of the Fifteenth World Conference on Earthquake Engineering (15 WCEE),* Lisbon, Portugal, September 24–28, 2012.

Anderson, D.P., 2004. BOINC: a system for public-resource computing and storage, in *Proceedings of the 5th IEEE/ACM International Workshop on Grid Computing,* Pittsburgh, USA.

Anderson, J.G., 1986. Implication of Attenuation for Studies of the Earthquake Source, in *Earthquake Source Mechanics,* American Geophysical Monograph 37, pp. 311–318, eds Das, S., Boatwright, J. & Scholz, C.H., AGU.

Anderson, J.G., 1991. A Preliminary descriptive model for the distance dependence of the spectral decay parameter in southern California, *Bull. seism. Soc. Am.,* **81**(6), 2186–2193.

Anderson, J.G. & Hough, S.E., 1984. A model for the shape of the Fourier amplitude spectrum of acceleration at high frequencies, *Bull. seism. Soc. Am.,* **74,** 1969–1993.

Anderson, J.G. & Lei, Y., 1994. Nonparametric description of peak acceleration as a function of magnitude, distance, and site in Guerrero, Mexico, *Bull. seism. Soc. Am.,* **84,** 1003–1017.

Anderson, J.G., Brune, J.N. & Wesnousky, S.G., 2002. Physical phenomena controlling high-frequency seismic wave generation in earthquakes, in *Proceedings of the 7th U.S. National Conf. on Earthquake Engineering,* Boston.

Arango, M.C., Strasser, F.O., Bommer, J.J., Boroschek, R., Comte, D. & Tavera, H., 2011. A strong-motion database from the Peru–Chile subduction zone, *J. Seismol.,* **15,** 19–41.

Atkinson, G.M., 1996. The high-frequency shake of the source spectrum for earthquakes in eastern and western Canada, *Bull. seism. Soc. Am.,* **86**(1A), 106–112.

Boore, D.M., 2004. Can site response be predicted?, *J. Earthq. Eng.,* **8,** 1–41.

Campbell, K.W., 2009. Estimates of shear-ave Q and $\kappa 0$ for unconsolidated and semiconsolidated sediments in eastern North America, *Bull. seism. Soc. Am.,* **99,** 2365–2392.

Castro, R.R., Anderson, J.G. & Singh, S.K., 1990. Site response, attenuation, and source spectra of S-waves along the Guerrero, Mexico, subduction zone, *Bull. seism. Soc. Am.,* **80,** 1481–1503.

Castro, R.R., Trojani, L., Monachesi, G., Mucciarelli, M. & Cattaneo, M., 2000. The spectral decay parameter κ in the region of Umbria-Marche, Italy, *J. geophys. Res.,* **105,** 23 811–23 823.

Chung, A.I. *et al.,* 2011. The quake-catcher network rapid aftershock mobilization project following the 2010 M8.8 Maule, Chile earthquake, *Seismol. Res. Lett.,* **82,** 526–532.

Chung, A.I., Cochran, E.S., Kaiser, A.E., Christensen, C.M., Yildirim, B. & Lawrence, J.F., 2014. Improved rapid magnitude estimation for a community-based, low-cost MEMS accelerometer network, *Bull. seism. Soc. Am.,* in press.

Cochran, E.S., Lawrence, J.F., Christensen, C. & Chung, A., 2009a. A novel strong-motion network for community participation in earthquake monitoring, *IEEE Instrument. Meas. Mag.,* **12**(6), 8–15.

Cochran, E.S., Lawrence, J.F., Christensen, C. & Jakka, R., 2009b. The quake-catcher network: citizen science expanding seismic horizons, *Seism. Res. Lett.,* **80,** 26–30.

Cochran, E.S., Lawrence, J.F., Kaiser, A., Fry, B., Chung, A.I. & Christensen, C., 2011. Comparison between low-cost and traditional MEMS accelerometers: a case study from the M7.1 Darfield, New Zealand, aftershock deployment, *Ann. Geophys.,* **54,** 728–737.

Cotton, F., Scherbaum, F., Bommer, J.J. & Bungum, H., 2006. Criteria for selecting and adjusting ground-motion models for specific target regions: application to Central Europe and rock sites, *J. Seism.,* **10,** 137–156.

DeMets, C., Gordon, R.G., Argus, D.F. & Stein, S., 1990. Current plate motions, *Geophys. J. Int.,* **101,** 425–478.

Douglas, J., Gehl, P., Bonilla, L.F. & Gelis, C., 2010. A κ model for mainland France, *Pure appl. Geophys.,* **167,** 1303–1315.

Drouet, S., Chevrot, S., Cotton, F. & Souriau, A., 2008. Simultaneous inversion of source spectra, attenuation parameters, and site responses: application to the data of the French Accelerometric Network, *Bull. seism. Soc. Am.,* **98,** 198–219.

Edwards, B., Fah, D. & Giardini, D., 2011. Attenuation of seismic shear wave energy in Switzerland, *Geophys. J. Int.,* **185,** 967–984.

Evans, J.R., Allen, R.M., Chung, A.I., Cochran, E.S., Guy, R., Hellweg, M. & Lawrence, J.F., 2014. Performance of several low-cost accelerometers, *Seism. Res. Lett.,* **85**(1), 147–158.

Federal Emergency Management Agency, 1997. NEHRP recommended provisions for seismic regulations for new buildings, FEMA 302, Washington, DC.

Fernández, A.I., Castro, R.R. & Huerta, C.I., 2010. The spectral decay parameter kappa in northeastern Sonora, Mexico, *Bull. seism. Soc. Am.,* **100,** 196–206.

Gentili, S. & Franceschina, G., 2011. High frequency attenuation of shear waves in the southeastern Alps and northern Dinarides, *Geophys. J. Int.,* **185,** 1391–1416.

Hanks, T.C., 1982. f_{max}, *Bull. seism. Soc. Am.,* **72,** 1867–1879.

Harris, R.A. & Day, S.M., 1997. Effects of a low-velocity zone on a dynamic rupture, *Bull. seism. Soc. Am.,* **87,** 1267–1280.

Hicks, S.P., Rietbrock, A., Haberland, C.A., Ryder, I.M.A., Simons, M. & Tassara, A., 2012. The 2010 M_w 8.8 Maule, Chile earthquake: nucleation and rupture propagation controlled by a subducted topographic high, *Geophys. Res. Lett.,* **39,** L19308, doi:10.1029/2012GL053184.

Jo, N. & Baag, C.-E., 2007. Estimation of site-dependent spectral decay parameter from earthquake ground motions in southern Korea, *Geosci. J.,* **11,** 165–174.

Jónsson, S., Zebker, H., Segall, P. & Amelung, F., 2002. Fault slip distribution of the 1999 Mw 7.1 hector mine, California, earthquake, estimated from satellite radar and GPS measurements, *Bull. seism. Soc. Am.,* **92,** 1377–1389.

Kilb, D., Biasi, G., Anderson, J., Brune, J., Peng, Z. & Vernon, F.L., 2012. Comparison of spectral parameter kappa from small and moderate earthquakes using southern California ANZA seismic network data, *Bull. seism. Soc. Am.,* **102,** 284–300.

Knopoff, L., 1964. Q, *Rev. Geophys.,* **2,** 625–660.

Ktenidou, O.-J., Gélis, C. & Bonilla, L.-F., 2013. A study on the variability of kappa (κ) in a borehole: implications of the computation process, *Bull. seism. Soc. Am.,* **103**(2A), 1048–1068.

Ktenidou, O.-J., Cotton, F., Abrahamson, N. & Anderson, J.G., 2014. Taxonomy of kappa: a review of definitions and estimation approaches targets to applications, *Seismol. Res. Lett.,* **85**(1), 135–146.

Lange, D. *et al.,* 2012. Aftershock seismicity of the 27 February 2010 Mw8.8 Maule earthquake rupture zone, *Earth planet. Sci. Lett.,* **317–318,** 413–425.

Laurendeau, A., Cotton, F., Ktenidou, O.-J., Bonilla, L.-F. & Hollender, F., 2013. Rock and stiff-soil site amplification: dependency on V_{s30} and kappa (κ_0), *Bull. seism. Soc. Am.,* **103**(6), 3131–3148.

Lawrence, J.F. *et al.,* 2014. Rapid earthquake characterization using MEMS accelerometers and volunteer hosts following the M 7.2 Darfield, New Zealand, earthquake, *Bull. seism. Soc. Am.,* **104**(1), 184–192.

Lay, T. & Wallace, T.C., 1995. *Modern Global Seismology,* Vol. 58, International Geophysics Series, Academic Press.

Meltzer, A. *et al.,* 2010. IRIS Community response to the Great Chile earthquake of 2010, in *Proceedings of the American Geophysical Union, Fall Meeting 2010,* abstract #G33A-0811, San Francisco, CA.

Myers, S.C., Beck, S., Zandt, G. & Wallance, T., 1998. Lithospheric-scale structure across the Bolivian Andes from tomographic images of velocity and attenuation for P and S waves, *J. geophys. Res.,* **103**(B9), 21 233–21 252.

Papageorgiou, A.S. & Aki, K., 1983. A specific barrier model for the quantitative description of inhomogeneous faulting and the prediction of strong ground motion, *Bull. seism. Soc. Am.,* **73,** 693–722.

Parolai, S. & Bindi, D., 2004. Influence of soil-layer properties on κ evaluation, *Bull. seism. Soc. Am.,* **94,** 349–356.

Purvance, M.D. & Anderson, J.G., 2003. A comprehensive study of the observed spectral decay in strong-motion accelerations recorded in Guerrero, Mexico, *Bull. seism. Soc. Am.,* **93,** 600–611.

Rovelli, A., Bonamassa, O., Cocco, M., Bona, M. & Mazza, S., 1988. Scaling laws and spectral parameters of the ground motion in active extensional areas in Italy, *Bull. seism. Soc. Am.,* **78**(2), 530–560.

Schurr, B., Asch, G., Rietbrock, A., Trumbull, R. & Haberland, C., 2003. Complex patterns of fluid and melt transport in the central Andean subduction zone revealed by attenuation tomography, *Earth planet. Sci. Lett.,* **215,** 105–119.

Servicio Nacional de Geologia y Mineria, 1982. Mapa geológico de Chile 1 : 1,000,000.

Toro, G., Abrahamson, A. & Schneider, J., 1997. Model of strong ground motions from earthquakes in the central and eastern North America: best estimates and uncertainties, *Seismol. Res. Lett.,* **68,** 41–57.

Tsai, C.-C.P. & Chen, K.-C., 2000. A model for the high-cut process of strong-motion accelerations in terms of distance, magnitude, and site condition: an example from the SMART 1 Array, Lotung, Taiwan, *Bull. seism. Soc. Am.,* **90,** 1535–1542.

Van Houtte, C., Drouet, S. & Cotton, F., 2011. Analysis of the origins of κ (Kappa) to compute hard rock to Rock adjustment factors for GMPEs, *Bull. seism. Soc. Am.,* **101,** 2926–2941.